Inserting Cr_2O_3 dramatically promotes RuO_2/TiO_2 catalyst for low-temperature 1,2-dichloroethane deep destruction: Catalytic performance and synergy mechanism

Yu Huang [a,b,1], Mingjiao Tian [a,c,1], Zeyu Jiang [a,d], Mudi Ma [a], Changwei Chen [a], Han Xu [a], Jingjie Zhang [a], Reem Albilali [e], Chi He [a,*]

[a] State Key Laboratory of Multiphase Flow in Power Engineering, School of Energy and Power Engineering, Xi'an Jiaotong University, Xi'an 710049, Shaanxi, PR China
[b] College of Geology and Environment, Xi'an University of Science and Technology, Xi'an 710054, Shaanxi, PR China
[c] Department of Materials Science and Engineering, National University of Singapore, Singapore 117575, Singapore
[d] Department of Chemistry, National University of Singapore, Singapore 117534, Singapore
[e] Department of Chemistry, College of Science, Imam Abdulrahman Bin Faisal University, P.O. Box 1982, Dammam 31441, Saudi Arabia

ARTICLE INFO

ABSTRACT

Ru-based catalysts with increased attention for CVOC purification still have huge challenges in promoting their low-temperature activity and durability. Here, a Cr-modified RuO_2/TiO_2 catalyst was fabricated and employed for 1,2-dichloroethane (1,2-DCE) destruction. The synergy of Cr_2O_3 and RuO_2/TiO_2 enhances the exposure of surface Ru, generating abundant reducible Cr^{6+} and Ru^{4+} species and chemically adsorbed oxygen, which promote the activity and CO_2/HCl selectivity in 1,2-DCE decomposition evidently. 1,2-DCE primarily activates on the Lewis acid sites (LAS) over $RuO_2/Cr_2O_3/TiO_2$ with C-Cl cleavage. Meanwhile, C-C cleavage occurs along with the dehydrochlorination and chlorination reactions. The presence of Cr_2O_3 greatly improves the LAS concentration and redox ability of RuO_2/TiO_2, accelerating the deep destruction of 1,2-DCE and inhibiting the formation of CH_2Cl_2, C_2HCl_3 and $CHCl_3$. Cr species with superior chlorine resistance elevate the durability of $RuO_2/Cr_2O_3/TiO_2$ under simulated conditions toward H_2O, SO_2, and chlorine species, making it a promising candidate for industrial CVOC catalytic degradation.

1. Introduction

Chlorinated volatile organic compounds (CVOCs) emitted from industrial processes cause a remarkably negative influence on the atmospheric environment and human health due to their severe toxicity, long durability and carcinogenicity [1]. Recently, the restrictions of CVOC emissions are more rigorous based on environmental protection regulations, and therefore, it is urgent to develop economical and feasible methods for CVOC elimination. Catalytic degradation has been identified as a cost-effective method for CVOC elimination owing to its high performance and environmental safety and elevated selectivity [2,3]. The development of reliable catalysts with superior catalytic performance and by-products inhibition ability is the key point for the efficient CVOC control.

Generally, supported noble metals, zeolites/modified zeolites and transition metal oxides are adopted as three major types of catalysts for CVOC degradation. Zeolites/modified zeolites present good activity and products selectivity, but their extensive application is restricted due to inevitable deactivation mainly caused by coke deposition [4,5]. Transitional metal oxides with the advantages of high availability and good resistance to chlorine poisoning have been widely investigated, whereas enhancing their low-temperature activity is still a challenge for CVOC elimination [6,7]. Supported noble metal catalysts with superior catalytic performance, high CO_x selectivity and regenerated ability have been extensively researched and applied for VOC elimination [8]. However, catalyst poisoning, deactivation and abundant chlorinated by-products generation over these catalysts greatly limit their practical application [9,10]. Comparatively, the Ru-based catalysts have advantages of excellent electron transfer capacity between metal and support and satisfied low-temperature redox ability (180–300 °C), offering them

---

a higher catalytic activity than Pt/Pd/Rh-based catalysts in CVOC degradation. One of such example has been reported by Miranda et al. [11], they pointed out that although Ru/Al$_2$O$_3$ has a higher trichloroethene (TCE) oxidation activity than that of Pd/Al$_2$O$_3$, Rh/Al$_2$O$_3$ and Pt/Al$_2$O$_3$ catalysts, it still has a low catalytic activity with T_{50} (temperature corresponding to 50% conversion of TCE) over 300 °C. In a later work, Liu et al. [12] observed that Ru/TiO$_2$ showed the highest activity and CO$_2$ selectivity among Pd/TiO$_2$, Rh/TiO$_2$ and Pt/TiO$_2$ catalysts for chlorobenzene (CB) degradation; more importantly, chlorine can be easily removed from the surface of Ru/TiO$_2$ through the Deacon process. However, RuOCl$_x$ species as active sites can be still formed during CB degradation, resulting in the formation of substantial hazardous polychlorinated benzene (PhCl$_x$) by-products. To meet the practical applications, improving the low-temperature activity and

reaction stability is still urgent to be resolved for Ru-based catalysts in CVOC degradation.

The introduction of transition oxide is a feasible strategy to enhance the activity of Ru-based catalysts. Wang et al. [13] have claimed that the introduction of Co species to Ru/Al$_2$O$_3$ can largely improve the oxygen mobility and the strong interaction between Co and Ru species can accelerate the electron transfer in RuCoO$_x$ active sites, promoting the catalytic activity in vinyl chloride degradation (T_{90} = 345 °C). It was also reported that the loading of V$_2$O$_5$ enhances the activity and stability of RuO$_2$/TiO$_2$ in dichloromethane degradation as V$_2$O$_5$ improves the acidic concentration of TiO$_2$ and thus accelerates the adsorption of dichloromethane and activation of C-Cl bonds; however, Cl$_2$ as the main inorganic chlorinated product almost unchanged compared to that of RuO$_2$/TiO$_2$ [14]. It has been previously reported that Cr$_2$O$_3$-supported
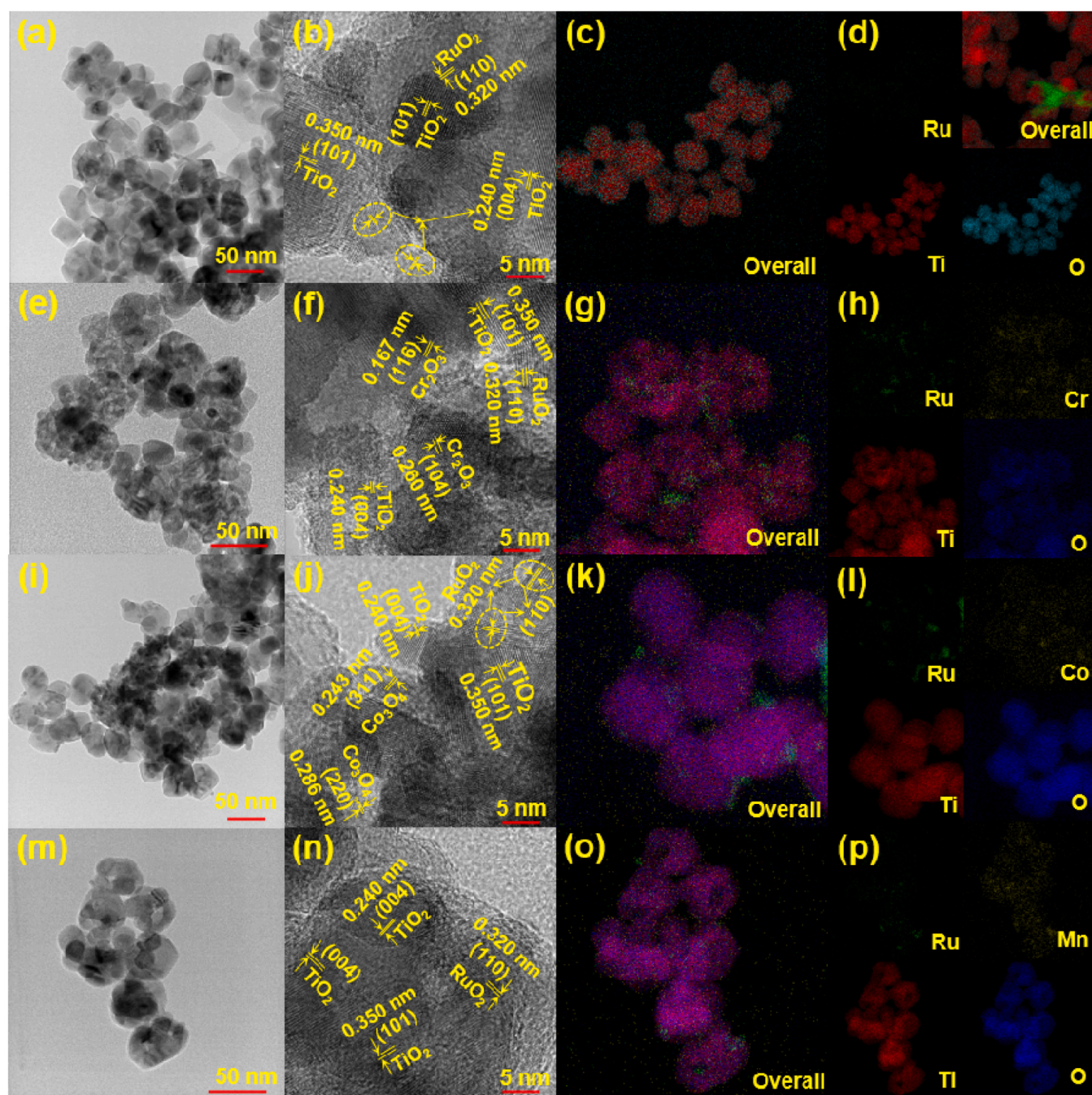

Fig. 1. TEM, HR-TEM, and EDS images of (a-d) RuTi, (e-h) RuCrTi, (i-l) RuCoTi, and (m-p) RuMnTi catalysts.
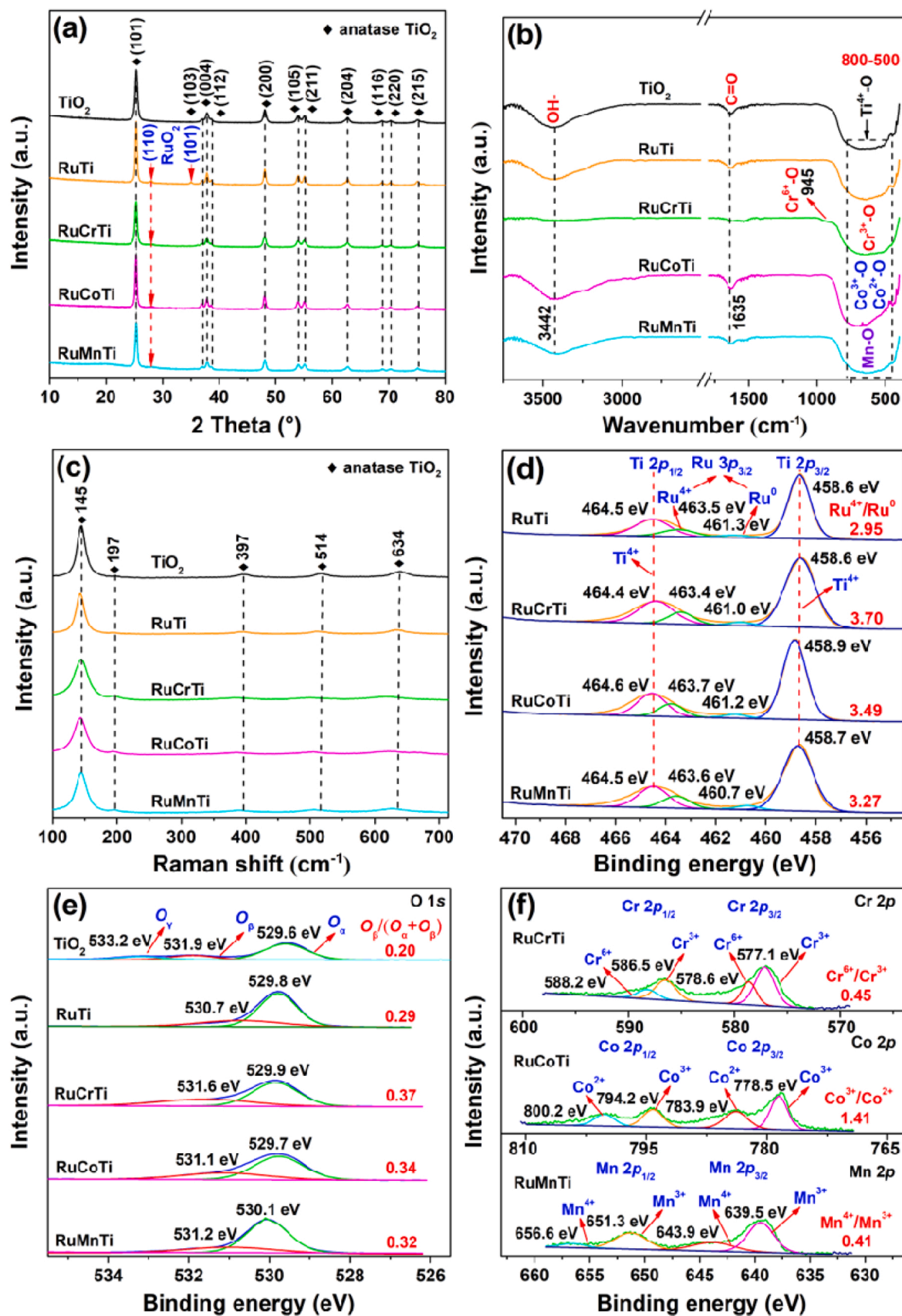
Fig. 2. (a) XRD, (b) FT-IR, (c) Raman and (d-f) XPS results of prepared catalysts.

catalysts with superior chlorine-resistance are one category of efficient materials for CVOC destruction attribute to their high HCl selectivity and high efficiency in the destruction of chlorinated by-products [3,15]. It is therefore logically to hypothesize that a catalyst coupled the advantages of both Cr_2O_3 and RuO_2/TiO_2 might be highly efficient in CVOC deep degradation.

For this, a $RuO_2/Cr_2O_3/TiO_2$ composite material was rationally fabricated by a simple wetness impregnation approach and adopted for 1,2-dichloroethane (1,2-DCE) catalytic degradation. The physicochemical property (*i.e.*, structure, reducibility, oxygen mobility and acidity) and catalytic performance (activity, reaction stability, and resistance to chlorine, SO_2 and H_2O) of prepared catalyst were systematically explored and compared with those of $RuO_2/MO_x/TiO_2$ (M = Co and Mn) and MO_x/TiO_2 (M = Cr, Co and Mn) catalysts. The selectivity of final inorganic products (CO_2, CO, HCl and Cl_2) and the distribution of chlorinated by-products were also investigated. Based on these findings, an intrinsic 1,2-DCE degradation mechanism over $RuO_2/Cr_2O_3/TiO_2$ catalyst was further proposed.

2. Experimental

2.1. Catalyst preparation

The MO_x (M = Cr, Co and Mn)/TiO_2 (denoted as MTi) catalysts were prepared using a wet impregnation method. Specifically, 3.0 g of commercial anatase TiO_2 was dispersed into deionized water under vigorous stirring for 0.5 h. A certain amount of metal nitrate (metal/Ti = 0.08/1; molar ratio) was then added to the above solution under vigorous stirring for another 0.5 h. The mixture was transferred to a water bath (60 °C) and completely evaporated under continuous stirring. Finally, the sample was calcined at 500 °C for 4 h to obtained the CrTi, CoTi and MnTi catalysts.

For the synthesis of $RuO_2/MO_x/TiO_2$ catalysts, 3.0 g of prepared MO_x/TiO_2 was dispersed into deionized water with vigorous stirring to form a uniform suspension solution. Next, 0.1776 g of $RuCl_3$ (35 wt%; theoretical content of 1 wt%) was added to the suspension solution and kept stirring at 60 °C until the excess water was completely removed, and then the sample was calcined at 500 °C for 4 h. The obtained catalysts were denoted as RuCrTi, RuCoTi, RuMnTi, and RuTi, respectively.

2.2. Catalyst characterizations

The prepared catalysts were characterized by X-ray diffraction (XRD), high-resolution transmission electron microscopy (HR-TEM), low-temperature nitrogen sorption, Fourier transform infrared spectroscopy (FTIR), X-ray photoelectron spectroscopy (XPS), Raman, H_2 temperature-programmed reduction (H_2-TPR), $O_2/NH_3/CO_2$ temperature-programmed desorption (O_2-TPD/NH_3-TPD/CO_2-TPD), FT-IR spectroscopy for NH_3 adsorption (NH_3-IR), and *in situ* diffuse reflectance infrared Fourier transform spectroscopy (*in situ* DRIFTS). The detailed information can be found in Text S1 (Supplementary Materials).

2.3. Catalytic activity

The activity of prepared catalysts for 1,2-DCE degradation was evaluated in a continuous flow quartz tube reactor (I.D. = 10 mm) under atmospheric pressure. During each test, 500 mg of catalyst (40–60 mesh) was packed into the tube reactor. The simulated exhaust gas (consisted of 1000 ppm 1,2-DCE; 21% O_2 and 79% N_2) was continually kept at 250 mL·min^{-1} (gas hourly space velocity of 30,000 mL·g^{-1}·h^{-1}). The online gas chromatograph (GC9890, China) equipped with an electron capture detector (ECD) was adopted to examine the concentrations of 1,2-DCE and chlorinated by-products. The concentrations of CO_x (CO and CO_2) were measured by the same chromatograph with a flame ionization detector (FID). The concentrations of HCl and Cl_2 were monitored online by HCl and Cl_2 detectors (PN-2000, China).

The 1,2-DCE conversion ($X_{1,2\text{-DCE}}$) was calculated by Eq. (1):

$$X_{1-\text{DCE}} = \frac{C_{in} - C_{out}}{C_{in}} \times 100\% \tag{1}$$

where C_{in} and C_{out} are the 1,2-DCE concentrations at the inlet and outlet, respectively.

The selectivity of CO, CO_2, HCl and Cl_2 (denoted as S_{CO}, S_{CO2}, S_{HCl} and S_{Cl2}, respectively) was calculated by Eqs. (2–5):

$$S_{CO} = \frac{C_{CO}}{2 \times C_{in} \times X_{1,2-\text{DCE}}} \times 100\% \tag{2}$$

$$S_{CO_2} = \frac{C_{CO_2}}{2 \times C_{in} \times X_{1,2-\text{DCE}}} \times 100\% \tag{3}$$

$$Y_{HCl} = \frac{C_{HCl}}{2 \times C_{in} \times X_{1,2-\text{DCE}}} \times 100\% \tag{4}$$

$$Y_{Cl_2} = \frac{C_{Cl_2}}{C_{in} \times X_{1,2-\text{DCE}}} \times 100\% \tag{5}$$

where C_{CO}, C_{CO2}, C_{HCl} and C_{Cl2} are the concentration of CO, CO_2, HCl, Cl_2 at the outlet, respectively.

The stability of catalysts was measured at T_{90} (temperature corresponding to 90% conversion of 1,2-DCE). Considering the effect of water vapor on catalytic performance, water vapor with different concentrations (1, 3 and 5 vol%) was respectively introduced into the simulated gas using an automatic injector. Additionally, to investigate the SO_2 resistance of RuCrTi catalyst, different concentrations of SO_2 (50 and 100 ppm) were added into the simulated gas and the catalytic performance was recorded on line.

3. Results and discussion

3.1. Structural and textural properties

Fig. 1 and S1 display the TEM, HR-TEM, and EDS images of catalysts. It is revealed that the shape of TiO_2 support keeps unchanged after impregnating of Ru and/or MO_x. All catalysts exhibit two types of lattice spacing of 0.350 and 0.240 nm, which are attributed to the (101) and (004) planes of TiO_2, respectively [16,17]. The (110) planes of RuO_2 with lattice spacing of 0.320 nm can be observed over RuTi and RuMTi catalysts [18]. Meanwhile, the EDS maps illustrated that Ru species are highly dispersed over RuTi and RuMTi catalysts (Fig. 1). As shown in Table S1, the dispersion of Ru over RuCrTi (49.0%) is higher than that of RuTi (41.5%), RuCoTi (46.2%) and RuMnTi (43.4%). For RuCrTi, the lattice spacings measured at 0.167 and 0.260 nm can be identified to the (116) and (104) planes of Cr_2O_3, respectively (Fig. 1f) [19,20]; however, only the (104) planes of Cr_2O_3 can be found over CrTi catalyst (Fig. S1f). Fig. 1j exhibits that both (311) and (220) planes of Co_3O_4 with lattice spacings respectively of 0.243 and 0.286 nm can be observed over RuCoTi catalyst, while the (311) and (111) planes (lattice spacing of 0.468 nm) of Co_3O_4 are detected over CoTi catalyst (Fig. S1j) [21]. The lattice of manganese over RuMnTi and MnTi catalysts is overlaid by other species (Fig. 1n and S1n). EDS maps demonstrate that all transition metal species are uniformly distributed over MTi and RuMTi catalysts. Additionally, the average pore diameter, pore volume and BET surface area of prepared catalysts are all almost unchanged after loading of Ru and/or transition metal oxides, suggesting that they are not the factor determining the activity (Text S2 and Table S1).

The XRD patterns of prepared catalysts are exhibited in Fig. 2a and S3a. The lattice planes of all catalysts are well consistent to the anatase phase TiO_2 (JCPDS #21–1272). For RuTi catalyst, the peaks at 28.1° and 35.2° are respectively attributed to the (110) and (101) planes of RuO_2 (JCPDS #43–10271). However, only the peak corresponding to the (110) planes of RuO_2 at 28.1° can be detected over RuMTi catalysts. The

Table 1
Textural property of prepared catalysts.

Sample	Molar ratio			H_2 consumption[c] (mmol·g^{-1})	P_{co}[d] ($\times 10^4$)	P_{lo}[e] ($\times 10^4$)	P_{wa}[f]	P_{sa}[g]	CO_2 desorption peak
	Ru^{4+}/Ru^0	$O_\alpha/(O_\alpha + O_\beta)$[a]	M^y/M^x[b]						
TiO$_2$	/	0.20	/	2.02	3.24	5.23	414	408	/
CrTi	/	0.26	0.38	10.79	4.10	5.51	122	248	27.6
CoTi	/	0.23	1.39	9.74	3.56	13.60	149	162	/
MnTi	/	0.22	0.40	8.76	3.84	24.90	192	198	/
RuTi	2.95	0.29	/	11.78	4.40	7.19	164	137	26.5
RuCrTi	3.70	0.37	0.45	26.69	5.24	4.71	102	612	91.6
RuCoTi	3.49	0.34	1.41	24.35	4.88	6.50	173	189	45.4
RuMnTi	3.27	0.32	0.41	21.68	4.68	7.80	145	168	42.3

[a] O_α and O_β are the surface adsorbed oxygen species and lattice oxygen, respectively; [b] $M^y/M^x = Cr^{6+}/Cr^{3+}$, Co^{3+}/Co^{2+}, or Mn^{4+}/Mn^{3+}; [c] H_2 consumption amount below 600 °C over all catalysts; Desorption peak areas of [d] chemically adsorbed oxygen and [e] lattice oxygen species; Desorption peak areas of [f] weak acid and [g] strong acid.

above results illustrated that partial Ru species in RuMTi materials migrate into TiO$_2$ lattice and strengthen the interaction between RuO$_2$ and TiO$_2$ [3]. Moreover, the intensity of these peaks over RuMTi catalysts is weaker than that of RuTi catalyst, indicating that the RuO$_2$ active sites are better dispersed over RuMTi catalysts than that of RuTi. Besides, no diffraction peaks corresponding to the transition metal oxides can be observed, indicating that transition metal oxides are highly dispersed over the TiO$_2$ support.

Fig. 2b and S3b shows the FTIR spectra of prepared catalysts. The broad peaks at approximately 3442–3440 cm^{-1} are identified as the stretching vibrations of surface hydroxyl groups (-OH) and the bands at 1635–1633 cm^{-1} are ascribed to the stretching vibration of C═O [20, 22]. A broad band in 800–500 cm^{-1} range is related to the vibrations of Ti-O bond over TiO$_2$ [23]. The FTIR spectra of RuMTi and MTi catalysts are similar to those of TiO$_2$ in the same range. No bands corresponding to Ru-O can be detected over RuMTi and RuTi catalysts and need to be further investigated. For RuCrTi and CrTi catalysts, a weak band corresponding to Cr^{6+}-O bond can be found at 945 cm^{-1} [20,22]. However, in the range of 800–500 cm^{-1}, the vibrations of Cr^{3+}-O and Ti-O bonds are coexistent, which are difficult to be separated [22,23]. Similarly, the broad bands at 800–500 cm^{-1} over RuCoTi and CoTi catalysts are associated with the vibrations Co^{3+}-O, Co^{2+}-O and Ti-O bonds [20]. The bands at 800–500 cm^{-1} for RuMnTi and MnTi catalysts can be assigned to the vibrations of Mn-O and Ti-O bonds [24]. According to the results of TEM, XRD, and FT-IR (Figs. 1 and 2a, b), it is speculated that RuO$_2$ species are well dispersed on the surface of transition metal oxides and TiO$_2$, or the co-interface between transition metal oxides and TiO$_2$. Raman spectra were further conducted to investigate the structure of prepared catalysts, as presented in Fig. 2c and S3c. The peaks at 145–146, 197–203, 397–399, 514–516, and 634–637 cm^{-1} over prepared catalysts are attributed to the vibration of anatase TiO$_2$ [25,26]. The peaks corresponding to the Ru and/or transition metal oxides cannot be detected. The intensity of Raman spectra for MTi and RuMTi catalysts is lower than that of TiO$_2$ because TiO$_2$ surface is covered by Ru and/or transition metal oxides in the composite materials [26].

3.2. Surface composition and element status

The chemical status of prepared catalysts was studied, as displayed in Fig. 2d-f and S3d-f. Only Ti^{4+} presented at 463.7–464.6 (Ti 2$p_{1/2}$) and 458.3–458.9 eV (Ti 2$p_{3/2}$) can be observed over all catalysts (Fig. 2d and S3d) [3]. The Ru 3d spectra overlap with the C 1s signal, and thus, it is difficult to distinguish each other. The Ru 3p spectra were employed to analyze the chemical status of Ru species. Two peaks at 460.7–461.3 and 463.4–463.7 eV over Ru 3$p_{3/2}$ are respectively assigned to Ru^0 and Ru^{4+} [27]. The ratios of Ru^{4+}/Ru^0 are 2.95, 3.70, 3.49 and 3.27 for RuTi, RuCrTi, RuCoTi and RuMnTi materials, respectively (Table 1), suggesting that RuCrTi has the highest amount of surface RuO$_2$ species. The results also illustrate that transition metal oxides promote the transformation of Ru^0 to Ru^{4+} due to the electron transfer between Ru and

transition metal oxides. Additionally, the Ru^{4+}/Ru^0 ratio over RuCrTi is higher than that of RuCoTi and RuMnTi materials, suggesting that the electron transfer effect between Ru and Cr is stronger than that of Co and Mn species. In other words, Ru species are more easily oxidized to high chemical states by Cr species compared to those of Co and Mn elements. During 1,2-DCE oxidation, the active electron transfers from Ru to Cr species, and then Cr species give electrons to O$_2$ in the atmosphere (obtaining active oxygen species (O$^-$ and O$_2^-$)) forming a redox reaction cycle, which benefits the effective degradation 1,2-DCE over RuO$_2$/Cr$_2$O$_3$/TiO$_2$ [28]. RuO$_2$ species are usually considered to be a redox center to accelerate the dissociation of 1,2-DCE and promote the removal of surface carbon and Cl species, and therefore enhance the stability of catalyst [10].

As shown in Fig. 2e and S3e, the O 1s spectra of prepared catalysts consist of three peaks at 529.5–530.1, 530.7–531.9, and 533.0–533.2 eV, which are respectively indexed to the lattice oxygen (O_α), surface adsorbed oxygen (O_β), and carbonates/adsorbed molecular water (O_γ) [20,22]. The ratio of $O_\beta/(O_\alpha + O_\beta)$ was calculated based on the areas of O_α and O_β, as listed in Table 1. The order of $O_\beta/(O_\alpha + O_\beta)$ ratio of prepared catalysts follows the sequence of RuCrTi (0.37) > RuCoTi (0.34) > RuMnTi (0.32) > RuTi (0.29) > CrTi (0.26) > CoTi (0.23) > MnTi (0.22) > TiO$_2$ (0.20). Generally, O_β is more active than that of O_α owing to its relatively higher mobility and lower surface bonding energy [29].

As displayed in Fig. 2f, the Cr 2$p_{3/2}$ spectra can be deconvoluted into two peaks corresponding to the Cr^{3+} (577.1 eV) and Cr^{6+} (578.6 eV), and the bands of Cr^{3+} and Cr^{6+} are respectively presented at 586.5 and 588.2 eV in the Cr 2$p_{1/2}$ spectra [3,20,22]. For Co 2p, the binding energy difference between Co 2$p_{3/2}$ and Co 2$p_{1/2}$ is approximately 15.4 eV, assigning to the Co$_3$O$_4$ spinel phase [22,30]. The Co 2$p_{3/2}$ spectra exhibit two peaks at 778.5 and 783.9 eV, which are respectively related to the Co^{3+} and Co^{2+}, and the Co^{3+} (794.2 eV) and Co^{2+} (800.2 eV) can also be observed in the Co 2$p_{1/2}$ spectra (Fig. 2f) [20,22]. Mn 2$p_{3/2}$ spectra are made up of Mn^{3+} (639.5 eV) and Mn^{4+} (643.9 eV), while Mn^{3+} (651.3 eV) and Mn^{4+} (656.6 eV) present in the Mn 2$p_{1/2}$ spectra [22, 31]. Figs. 2f, 3f and Table 1 show the ratios of Cr^{6+}/Cr^{3+}, Co^{3+}/Co^{2+} and Mn^{4+}/Mn^{3+} over RuCrTi (CrTi), RuCoTi (CoTi) and RuMnTi (MnTi) catalysts, respectively. Interestingly, the ratio of Cr^{6+}/Cr^{3+} obviously increases from 0.38 (RuTi) to 0.45 (RuCrTi) (Table 1), suggesting that Cr^{3+} is rapidly oxidized to Cr^{6+} by gas oxygen, which leads to the timely replenishment Cr^{6+} species and further promotes the formation of Ru^{4+} species [28].

3.3. Reducibility and oxygen species mobility

The reducibility of prepared catalysts was evaluated by H$_2$-TPR, as illustrated in Fig. 3a, b and S4a. For all catalysts, the peaks observed at > 500 °C are assigned to the reduction of Ti^{4+} to Ti^{3+} and combustion of lattice oxygen species [3,32]. The reduction peaks at 128–145 and 196–206 °C respectively correspond to the RuO$_2$ species strong and
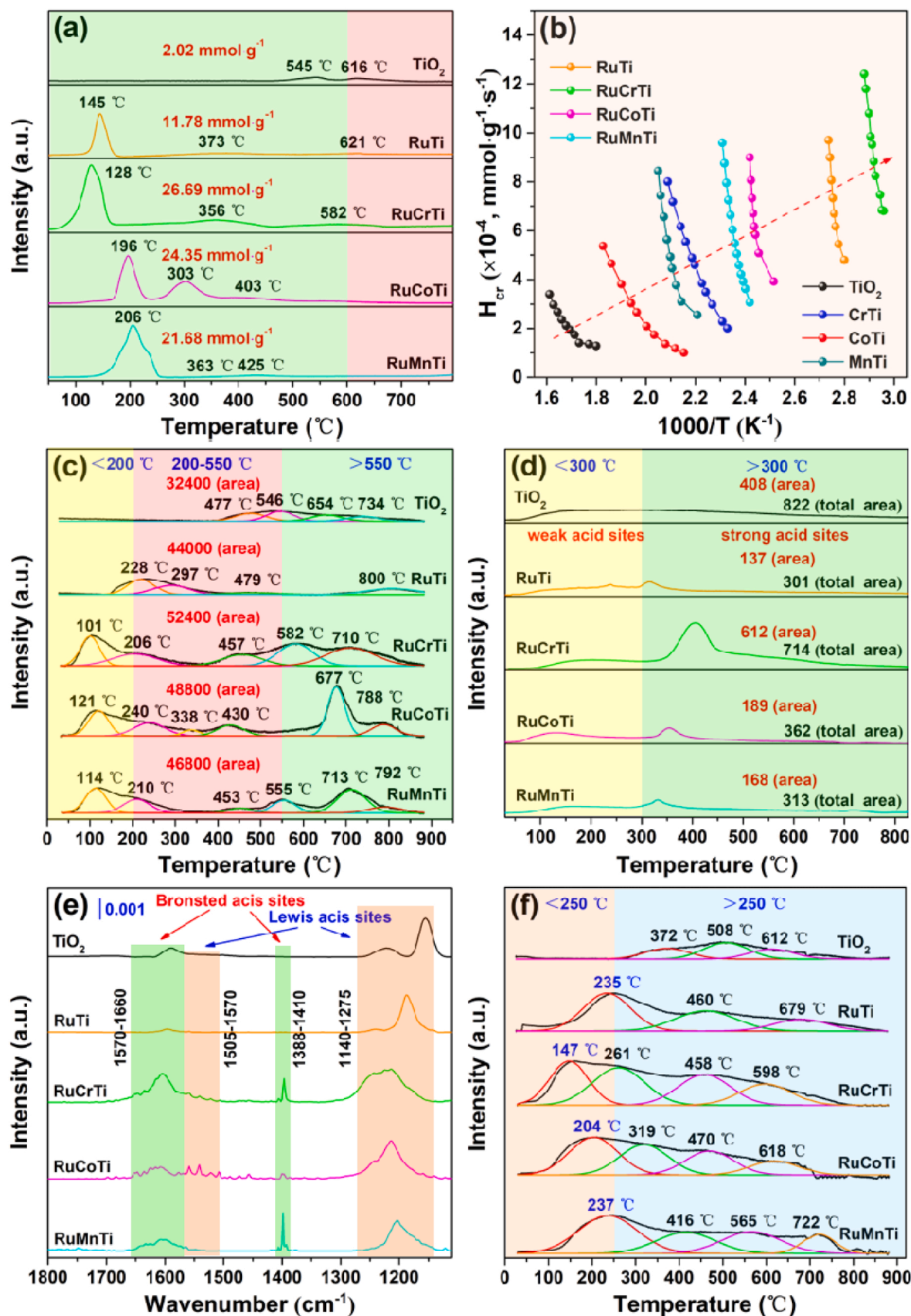
Fig. 3. (a) H$_2$-TPR, (b) H$_2$ consumption rate, (c) O$_2$-TPD, (d) NH$_3$-TPD, (e) NH$_3$-IR, and (f) CO$_2$-TPD of prepared catalysts.
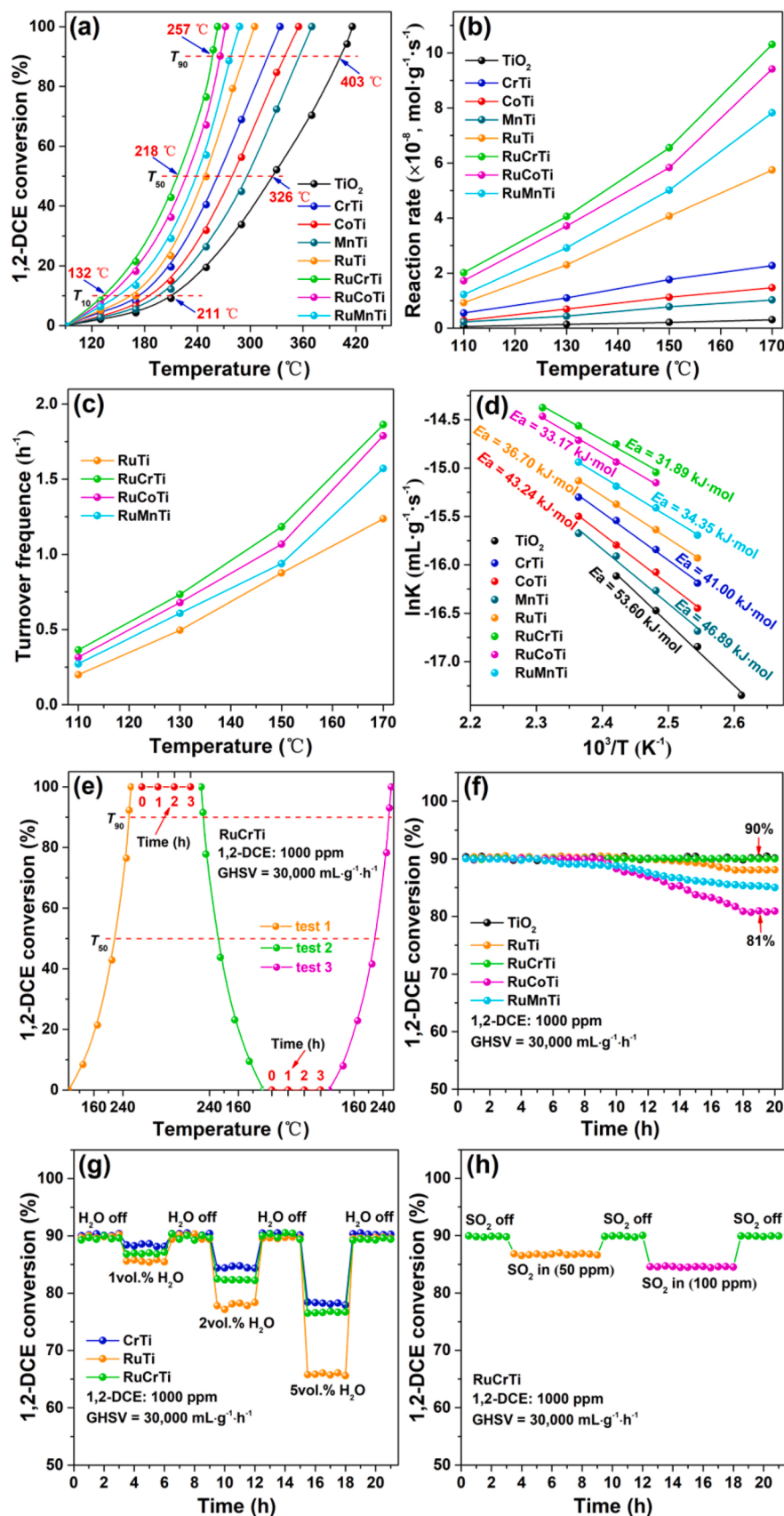
Fig. 4. (a) Catalytic activity, (b) reaction rate, (c) turnover frequency, and (d) apparent activation energy of prepared catalyst for 1,2-DCE decomposition; (e-f) Recycle activity and stability of prepared catalysts; (g) Effect of water vapor on prepared catalysts in 1,2-DCE decomposition; (h) Effect of SO₂ on RuCrTi catalyst in 1,2-DCE decomposition.

Table 2
Catalytic performance of prepared catalysts for 1,2-DCE degradation.

Sample	T_{10}[a] (°C)	T_{50}[a] (°C)	T_{90}[a] (°C)	R[b] (×10^{-8}, mol·g^{-1}·s^{-1})	TOF_{Ru}[c] (h^{-1})	E_a[d] (kJ·mol^{-1})	S_{CO2}[e] (%)	S_{CO}[e] (%)	S_{HCl}[e] (%)	S_{Cl2}[e] (%)
TiO$_2$	211	326	403	0.21	/	53.60	70.6	11.0	45.6	51.4
CrTi	173	264	321	1.77	/	41.00	92.2	6.9	79.8	17.7
CoTi	187	281	340	1.13	/	43.24	94.3	4.5	74.7	22.8
MnTi	197	292	358	0.78	/	46.89	77.7	15.6	67.9	28.1
RuTi	164	247	292	4.07	0.88	36.70	94.0	2.5	83.1	15.1
RuCrTi	132	218	257	6.55	1.18	31.89	99.1	0.2	94.0	4.9
RuCoTi	141	228	266	5.83	1.07	33.17	98.3	0.0	89.7	8.9
RuMnTi	150	239	278	5.02	0.94	34.35	94.5	3.8	85.9	12.3

[a] Temperatures at which 10%, 50% and 90% conversion of 1,2-DCE; [b] Reaction rate of 1,2-DCE transformed per surface area per unit time over various catalysts at 150 °C; [c] Turnover frequency based on the dispersion of Ru obtained at 150 °C; [d] Apparent activation energy obtained from the Arrhenius plots; [e] Selectivity of CO$_2$, CO, HCl and Cl$_2$ over all catalysts during 1,2-DCE degradation.

weak interacted with TiO$_2$ [33,34]. Compared to RuTi catalyst (145 °C), the initial reduction temperature of RuCrTi catalyst significantly shifts to a lower temperature (128 °C) after Cr$_2$O$_3$ loading, meaning that Cr$_2$O$_3$ can promote the reduction of Ru species. Interestingly, the initial reduction temperature of RuCoTi (196 °C) and RuMnTi (206 °C) catalysts is much higher than that of RuTi catalyst. For RuMTi and MTi catalysts, the peaks at 250–500 °C can be mainly ascribed to the reduction of transition metal oxides with different phases (Fig. 3a and S4a). For RuCrTi and CrTi catalysts, the peaks respectively at 356 and 305 °C are attributed to the reduction of Cr$_2$O$_3$ along with surface oxygen species, while the peak at 429 °C is corresponding to the reduction of Cr^{3+}/Cr^{2+} to metallic Cr [20,22]. The peaks at 300–400 and 400–500 °C can be respectively ascribed to the reduction of Co$_3$O$_4$ to CoO and CoO to metallic Co over RuCoTi and CoTi catalysts [20,35]. For RuMnTi and MnTi catalysts, the peaks at 363 and 372 °C are attributed to the reduction of Mn$_3$O$_4$ to MnO, and the peaks at 425 and 480 °C are indexed to the reduction of MnO to metallic Mn [19]. The corresponding H$_2$ consumption (< 600 °C) was calculated to quantitatively analyze the low-temperature reducibility of catalysts, as documented in Table 1. The amount of H$_2$ consumption follows the trend of RuCrTi (26.69 mmol·g^{-1}) > RuCoTi (24.35 mmol·g^{-1}) > RuMnTi (21.68 mmol·g^{-1}) > RuTi (11.78 mmol·g^{-1}) > CrTi (10.79 mmol·g^{-1}) > CoTi (9.74 mmol·g^{-1}) > MnTi (8.76 mmol·g^{-1}) > TiO$_2$ (2.02 mmol·g^{-1}), illustrating that RuCrTi exhibits the highest amount of H$_2$ consumption. The initial H$_2$ consumption rate (H_{cr}; the consumed oxygen less than 25% for the first reduction peak of catalyst) was estimated to compare the low-temperature reducibility, as displayed in Fig. 3b. RuCrTi catalyst exhibits the highest initial H$_2$ consumption rate among all catalysts. The above results reveal that the RuCrTi possesses the best reducibility among all prepared catalysts, which accelerates the transfer of oxygen species and activation of reactants [31].

As shown in Fig. 3c and S4b, the O$_2$-TPD spectra can be divided into three desorption regions. The peaks at temperatures < 200, 200–550 and > 550 °C are respectively assigned to the desorption of physically adsorbed oxygen, chemically adsorbed oxygen and lattice oxygen [35, 36]. In general, the chemically adsorbed oxygen species are more active than that of the lattice oxygen in 1,2-DCE deep degradation [35]. The amounts of chemically adsorbed oxygen over prepared catalysts were calculated by integral area, which decreases as RuCrTi (52400) > RuCoTi (48800) > RuMnTi (46800) > RuTi (44000) > CrTi (41000) > MnTi (38400) > CoTi (35600) > TiO$_2$ (32400), suggesting that RuCrTi has the highest amounts of active chemically adsorbed oxygen species.

3.4. Surface acidity

NH$_3$-TPD experiment was performed to study the acid property of prepared catalysts, as illustrated in Fig. 3d and S4c. The desorption peak at temperature below/above 300 °C corresponds to the NH$_3$ absorbed on weak/strong acid sites [3,29]. It is accepted that the strong acid sites are more favorable for CVOC deep oxidation than the weak acid sites [37].

The amounts of strong acid sites were calculated and shown in Table 1. The amount of strong acid sites follows the trend of RuCrTi (612) > TiO$_2$ (408) > CrTi (248) > MnTi (198) > RuCoTi (189) > RuMnTi (168) > CoTi (162) > RuTi (137), indicating that the presence of Cr$_2$O$_3$ introduces the highest quantity of strong acid sites to RuTi catalyst. Besides, the reduction of acid strength of Ru-based catalysts may be due to the blockage of partial surface acid sites by Ru species or weaken by Ru species with intrinsic weak basic [29,38]. NH$_3$-IR experiments were further employed to investigate the type of acid sites (Fig. 3e and S4d). The peaks at 1505–1570 and 1140–1275 cm^{-1} can be assigned to the Lewis acid sites (LAS), while the peaks at 1570–1660 and 1388–1410 cm^{-1} can be attributed to Brønsted acid sites (BAS) [20,22]. It is recognized that the LAS are conducive to the dissociative adsorption of Cl from CVOCs [39]. Apparently, the presence of Cr species in RuO$_2$/TiO$_2$ greatly improves the LAS amounts compared to other catalysts, which is favorable for the faster desorption of Cl from 1,2-DCE.

Fig. 3f and S4e show the CO$_2$-TPD profiles of prepared catalysts. Generally, the peak of weak basic sites can be observed with desorption temperatures lower than 250 °C, while the desorption peaks of medium/strength basic sites are in the range of 250–880 °C [3,40]. Fig. 3f shows that the peaks are consist of the weak basic sites (below 250 °C) and medium/strength basic sites (above 250 °C) over RuMTi and RuTi catalysts. However, only the peaks of medium/strength basic sites can be detected over MTi and TiO$_2$ catalysts (Fig. S4e). The amounts of weak basic sites follow the order of RuCrTi (91.6) > RuCoTi (45.4) > RuMnTi (42.3) > CrTi (27.6) > RuTi (26.5) (Table 1). It is found that the strength and amount of weak basic sites increase after the loading of transition metal oxide on RuTi catalysts, which is favorable to the desorption of CO$_2$ product [3].

3.5. Catalytic performance

3.5.1. Catalytic activity, stability and selectivity

It can be observed from Fig. 4a that the activity of prepared catalysts is clearly enhanced after the loading of RuO$_2$ and/or transition metal oxides, illustrating that the synergy between TiO$_2$, RuO$_2$ and transition metal oxides promotes the catalytic activity for 1,2-DCE destruction. The T_{10}, T_{50}, and T_{90} (temperatures corresponding to 10%, 50% and 90% conversion of 1,2-DCE) of catalysts are listed in Table 2 to better compare the activity of prepared catalysts. Based on T_{90}, the order of activity is RuCrTi (257 °C) > RuCoTi (266 °C) > RuMnTi (278 °C) > RuTi (292 °C) > CrTi (321 °C) > CoTi (340 °C) > MnTi (358 °C) > TiO$_2$ (403 °C). Compared to other catalysts, the temperatures of T_{50} and T_{10} of RuCrTi catalyst are also much lower, indicating that RuCrTi has an outstanding low-temperature activity. The reaction rates and TOF_{Ru} values were calculated to discuss the intrinsic activity of catalysts. As displayed in Fig. 4b and Table 2, the reaction rate of prepared catalysts at 150 °C follows the order of RuCrTi (6.55 ×10^{-8} mol·g^{-1}·s^{-1}) > RuCoTi (5.83 ×10^{-8} mol·g^{-1}·s^{-1}) > RuMnTi (5.02 ×10^{-8} mol·g^{-1}·s^{-1}) > RuTi (4.07 ×10^{-8} mol·g^{-1}·s^{-1}) > CrTi (1.77 ×10^{-8} mol·g^{-1}·s^{-1}) > CoTi (1.13 ×10^{-8} mol·g^{-1}·s^{-1}) > MnTi (0.78 ×10^{-8}
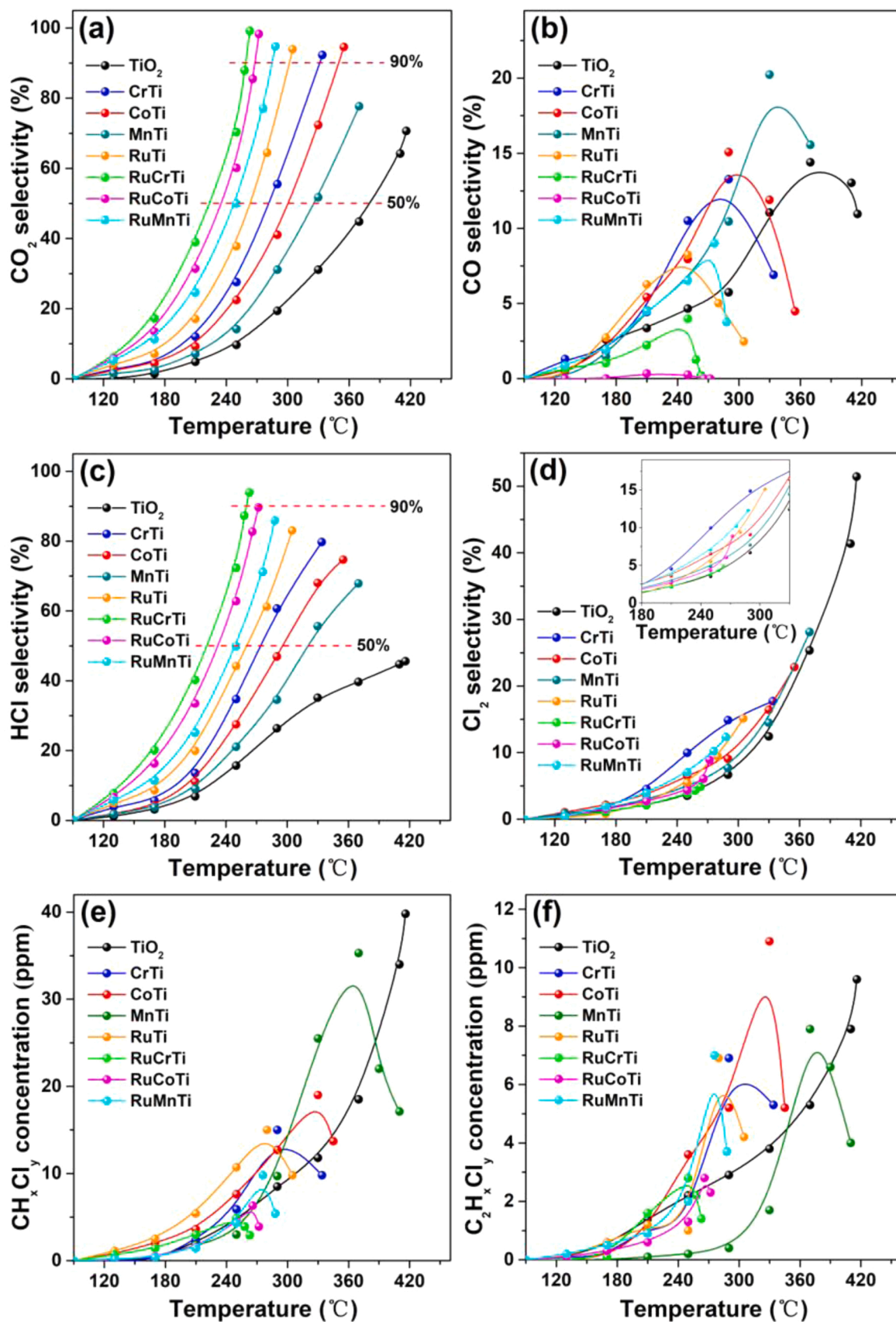
Fig. 5. Selectivity of (a) CO_2, (b) CO, (c) HCl, and (d) Cl_2 over prepared catalysts; (e-f) CH_xCl_y and $C_2H_xCl_y$ by-products concentrations over prepared catalysts.
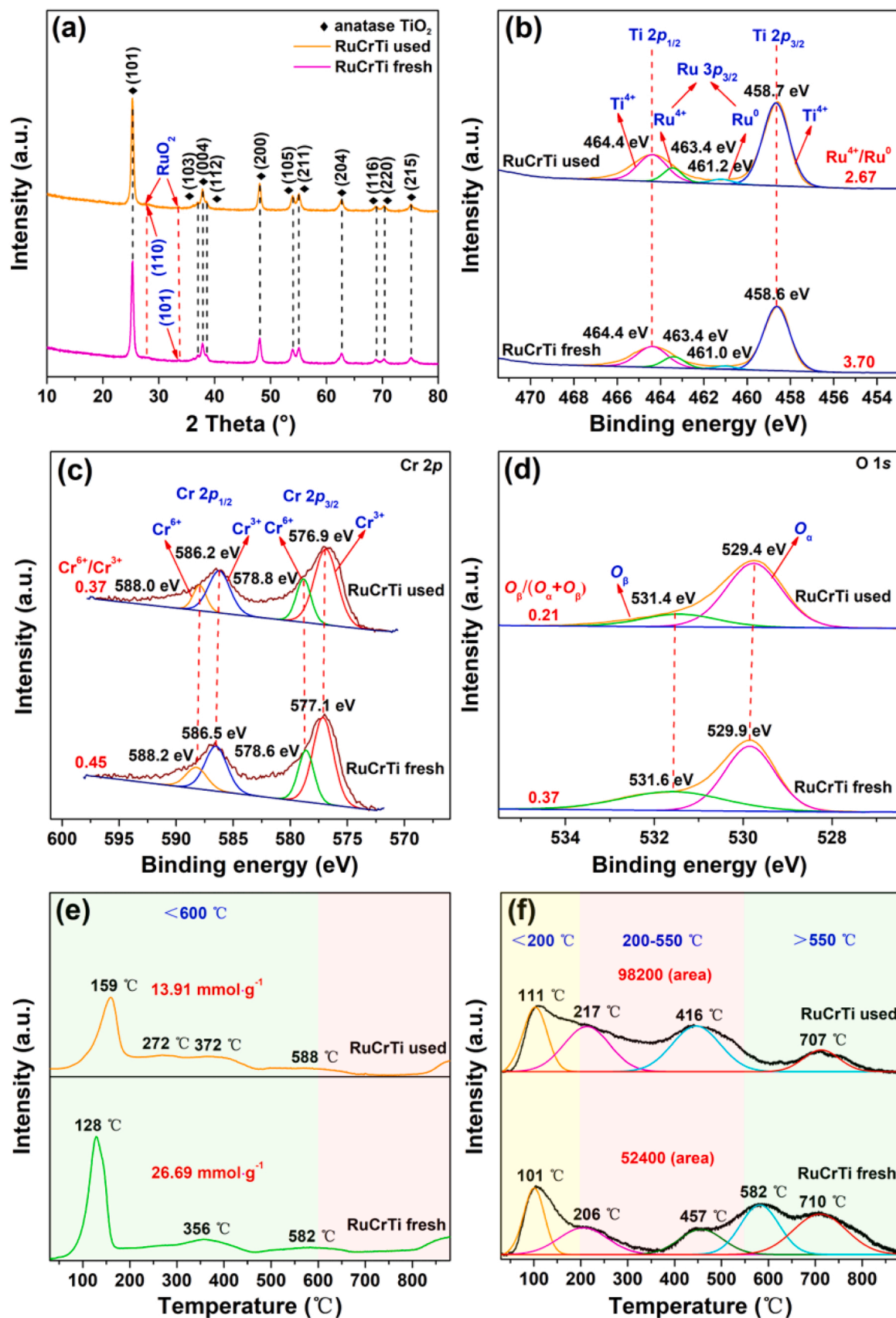
Fig. 6. (a) XRD, (b-d) XPS, (e) H$_2$-TPR, and (f) O$_2$-TPD of the fresh and used RuCrTi catalysts.

mol·g^{-1}·s^{-1}) > TiO$_2$ (0.21 ×10^{-8} mol·g^{-1}·s^{-1}). The TOF_{Ru} values of RuTi and RuMTi catalysts are also obtained and presented in Fig. 4c and Table 2. The TOF_{Ru} for RuTi, RuCrTi, RuCoTi and RuMnTi catalysts are 0.88, 1.18, 1.07 and 0.94 h^{-1}, respectively, demonstrating that the highest intrinsic activity of RuCrTi catalyst. To further evaluate the catalytic performance, the apparent activation energy (E_a) of prepared catalysts was calculated in the kinetics regime, as presented in Fig. 4d and Table 2. It is shown that RuCrTi catalyst exhibits the lowest E_a value (31.89 kJ·mol^{-1}) compared with the other catalysts (33.17–53.60 kJ·mol^{-1}), and the present of transition metal oxides can reduce the energy barriers in catalytic degradation of 1,2-DCE. The above results suggest that Cr$_2$O$_3$ boosts the synergy between RuO$_2$ and TiO$_2$ over RuCrTi catalyst than that of Co$_3$O$_4$ and Mn$_3$O$_4$.

The catalytic stability is an indispensable indicator for the potential application of prepared catalysts. As displayed in Fig. 4e, the activity of RuCrTi catalyst is almost unchanged during the whole testing period, indicating the superior catalytic activity of RuCrTi. In addition to this, the stability tests were conducted at temperatures corresponding to T_{90} of catalysts for 24 h (Fig. 4f and S5). Apparently, the 1,2-DCE conversion maintains steady over TiO$_2$, CrTi and RuCrTi catalysts, indicating that these catalysts possess considerable stability and chlorine resistance. However, significant activity losses can be observed over RuCoTi, RuMnTi, CoTi and MnTi catalysts after 24 h of continuous reaction due to the accumulation and deposition of Cl species over active sites, which cause the activity decrease and catalyst deactivation [41].

Investigating the effect of water on prepared catalysts has a great significance as H$_2$O is not only one of CVOC degradation products but usually exists in industrial waste gases. As shown in Fig. 4g, the presence of H$_2$O has a negative impact on the activity of these catalysts, and the activity decreases with increasing of H$_2$O concentrations from 1 to 5 vol % due to the competitive adsorption between H$_2$O and 1,2-DCE molecules. Remarkably, the decrease degree of activity for CrTi and RuCrTi catalysts is much lower than that of RuTi, indicating that the presence of Cr species can efficiently restrain the competitive adsorption between H$_2$O and 1,2-DCE molecules for RuTi catalyst [42,43]. Additionally, the activity of these catalysts keeps steady in the presence of water, and the activity can restore to the initial level when water vapor is absent.

SO$_2$ as a kind of common industrial waste gas was also explored to evaluate SO$_2$ tolerance of RuCrTi catalyst. As shown in Fig. 4h, the activity of RuCrTi catalyst decreases from 90% to 85% when a low concentration of SO$_2$ (50 ppm) is introduced, and the activity further decreases to 80% in the presence of 100 ppm of SO$_2$. It is deduced that the decrease of 1,2-DCE adsorption capacity of the catalyst after sulfuration and the competitive adsorption between SO$_2$ and 1,2-DCE molecules may be the reasons for activity reduction [38,42,43]. Moreover, the activity of RuCrTi catalyst was almost unchanged during the shock of SO$_2$. Importantly, the activity of RuCrTi can be well-recovered to the initial level (90%) when SO$_2$ is shut down.

The selectivity of final inorganic products (CO, CO$_2$, HCl and Cl$_2$) over prepared catalysts were analyzed, as shown in Fig. 5a-d and Table 2. The CO$_2$ selectivity (70.6–99.1%) over all catalysts is over 3 times higher than that of CO (0.0–15.6%). Meanwhile, the CO$_2$ selectivity over RuCrTi can reach up to 99.1% at 263 °C, obviously higher than the other catalysts (Fig. 5a and Table 2). According to Table 2, the order of CO$_2$ selectivity is RuCrTi (99.1%) > RuCoTi (98.3%) > RuMnTi (94.5%) > CoTi (94.3%) > RuTi (94.0%) > CrTi (92.2%) > MnTi (77.7%) > TiO$_2$ (70.6%), suggesting that the presence of RuO$_2$ and transition metal oxides enhances the mineralization rate of 1,2-DCE and organic intermediates. As shown in Fig. 5b, the CO selectivity over all catalysts initially increases and then decreases with the increasing of temperature due to the further oxidation of CO at elevated temperatures [1,20]. The selectivity of HCl and Cl$_2$ is exhibited in Fig. 5c, d and Table 2. As we all know, HCl is a more ideal product than Cl$_2$ due to its low toxicity and can be easily treated. It can be observed from Fig. 5c and Table 2 that the HCl selectivity (67.9–94.0%) is over 2 times higher than that of Cl$_2$ (4.9–28.1%) over all catalysts (except TiO$_2$). The order

of HCl selectivity is well consistent with the activity of RuCrTi (94.0%) > RuCoTi (89.7%) > RuMnTi (85.9%) > RuTi (83.1%) > CrTi (79.8%) > CoTi (74.7%) > MnTi (67.9%) > TiO$_2$ (45.6%) (Table 2). Moreover, the RuCrTi catalyst has the lowest Cl$_2$ selectivity (4.9%) owing to its superior low-temperature activity as Cl$_2$ is easily produced from HCl at high temperature *via* the Deacon reaction [12]. Besides, the presence of transition metal oxides increases the concentration of strong acid sites over RuTi catalyst, which accelerates C-Cl bonds dissociation and promotes the formation of HCl [1,44,45].

3.5.2. Intermediate distribution and proposed mechanism

As shown in Fig. S6, the concentrations of chlorine by-products (dichloromethane (CH$_2$Cl$_2$), trichloromethane (CHCl$_3$), perchloromethane (CCl$_4$), chloroethylene (C$_2$H$_3$Cl), trichloroethylene (C$_2$HCl$_3$) and trichloroethane (C$_2$H$_3$Cl$_3$)) initially increase and then decrease with the increasing of temperature over all catalysts (except TiO$_2$), meaning that chlorine by-products were further decomposed at high temperature. The concentration of chlorine by-products complete degradation of 1,2-DCE) decreases as the order of RuCrTi (4 ppm) < RuCoTi (6 ppm) < RuMnTi (9 ppm) < RuTi (14 ppm) < CrTi (15 ppm) < CoTi (19 ppm) < MnTi (21 ppm) < TiO$_2$ (49 ppm) (Table S2). It is demonstrated that the concentration of chlorine by-products over RuCrTi is the lowest among all catalysts for the complete destruction of 1,2-DCE. The concentration of chlorine by-products (4–9 ppm) for RuMTi catalysts is less than that of MTi catalysts (15–21 ppm), indicating that the strong oxidizing ability of RuO$_2$ is the main reason for the low concentration of chlorine by-products over RuMTi. Another reason can be attributed to that the transition metal oxides can promote the reducibility of the catalysts, leading to large amounts of inorganic chlorine products (HCl and Cl$_2$) formed and then rapidly removed from the surface. The concentrations of single-carbon chlorine by-products (3–40 ppm) are higher than those of double-carbon chlorine by-products (1–10 ppm) over all catalysts (Fig. 5e, f), illustrating that the cleavage of C-C bonds is the main reaction during the destruction of 1,2-DCE.

To further understand the reaction behavior of RuCrTi catalyst during 1,2-DCE degradation, the XRD, Ru 3p XPS, O 1s XPS, Cr 2p XPS, H$_2$-TPR and O$_2$-TPD of the used RuCrTi catalyst were analyzed. As shown in Fig. 6a, the corresponding characteristic peaks of the used RuCrTi catalyst maintain unchanged compared to the fresh one, illustrating that Cl species do not affect the structure of RuCrTi catalyst. Fig. 6b exhibits that the ratio of Ru^{4+}/Ru^0 of the used RuCrTi catalyst (2.67) is much lower than the fresh RuCrTi catalyst (3.70), suggesting that a large number of Ru^{4+} species participate in the reaction, which results in excellent activity for the deep oxidation of 1,2-DCE due to the strong oxidizing ability of RuO$_2$ (Ru^{4+} species are the main active sites of RuCrTi). It is seen that the Cr^{6+}/Cr^{3+} ratio (0.37) of the used RuCrTi catalysts is less than that of the fresh catalyst (0.45), suggesting that Cr species as the second active sites in RuCrTi take part in 1,2-DCE decomposition reaction (Fig. 6c). Meanwhile, the ratio of $O_\beta/(O_\alpha + O_\beta)$ over RuCrTi also decreases apparently from 0.37 to 0.21 after reaction, demonstrating that surface adsorbed oxygen species play an important role during 1,2-DCE decomposition (Fig. 6d). As shown in Fig. 6e, the amount of low-temperature H$_2$ consumption over the used catalysts (13.91 mmol·g^{-1}) is nearly one half of that over the fresh one (26.69 mmol·g^{-1}), indicating that the reducibility has a significantly influence on the low-temperature activity of RuCrTi. Fig. 6f exhibits more active surface oxygen species with high mobility are formed due to the oxygen species transfer from bulk to the surface of the catalysts, which can accelerate the reaction process. The above results also reveal that alternative oxidation and reduction on the surface of catalyst in the whole process favorable for the active surface oxygen species successive replenishment, and further promotes the effective oxidation of 1,2-DCE [46]. The behavior of chlorine species was also investigated by analyzing the Cl 2p spectra of the used catalysts, as displayed in Fig. S7. All catalysts exhibit two peaks at 197.9–198.7 and 199.8–200.1 eV, respectively, ascribed to the adsorbed HCl and adsorbed chlorinated
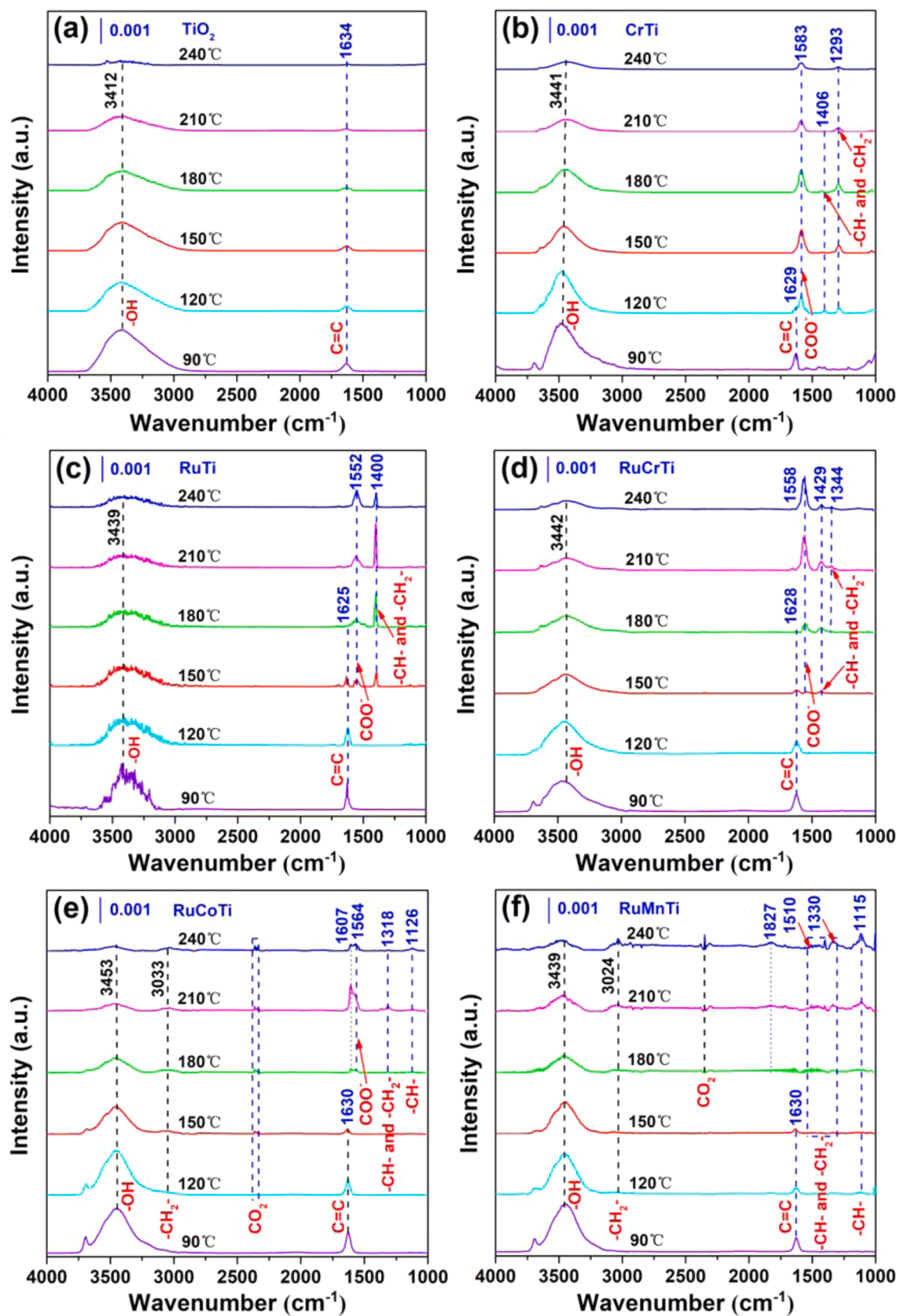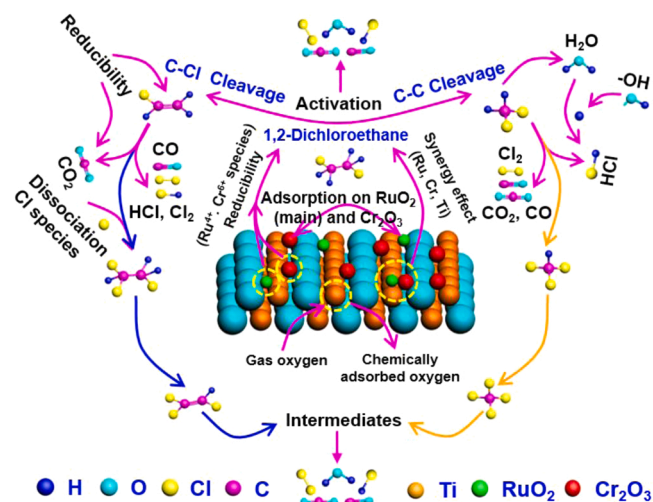
Fig. 7. *In situ* DRIFTS of 1,2-DCE catalytic destruction over prepared catalysts: (a) TiO₂, (b) CrTi, (c) RuTi, (d) RuCrTi, (e) RuCoTi, and (f) RuMnTi.

Scheme 1. Proposed 1,2-dichloroethane destruction mechanism over prepared catalysts.

organic species [20,22]. Obviously, RuCrTi has a lower amount of adsorbed Cl species compared to the other catalysts, illustrating that the effect of Cl species on RuCrTi catalyst is weaker due to the effective Cl species removal capability of Cr and Ru elements.

In situ DRIFTS were performed to investigate the reaction process at different temperatures, as presented in Fig. 7. The strong bands in $3453–3412 cm^{-1}$ can be considered as the vibration of OH over all catalysts, and the intensity of these bands decreases with the increasing of temperature [20,22]. For RuCoTi and RuMnTi catalysts, the bands at $3033–3024 cm^{-1}$ are indexed to $-CH_2-$ stretching, while the weak bands corresponding to CO_2 adsorption can be detected at $2400–2300 cm^{-1}$ [47]. Interestingly, no bands of -CH- stretching vibrations for formaldehyde species at $2979–2840 cm^{-1}$ can be detected over all catalysts [48]. The bands at $1634–1625 cm^{-1}$ appeared over prepared catalysts, which ascribe to C=C stretching vibration [20,22]. The vibration of hydroxyl in water with a band at $1607 cm^{-1}$ originated from the oxidation of adsorbed species only present in RuCoTi catalyst [48]. The bands at $1583–1552 cm^{-1}$ are indexed to the COO^- asymmetric stretching over CrTi, RuTi, RuCrTi and RuCoTi catalysts, meaning the generation of surface acetate species [20,22]. The bands at $1510–1290 cm^{-1}$ are assigned to the $-CH_2-$ and/or -CH- vibration, meaning that 1,2-DCE is adsorbed and activated [47]. Additionally, the
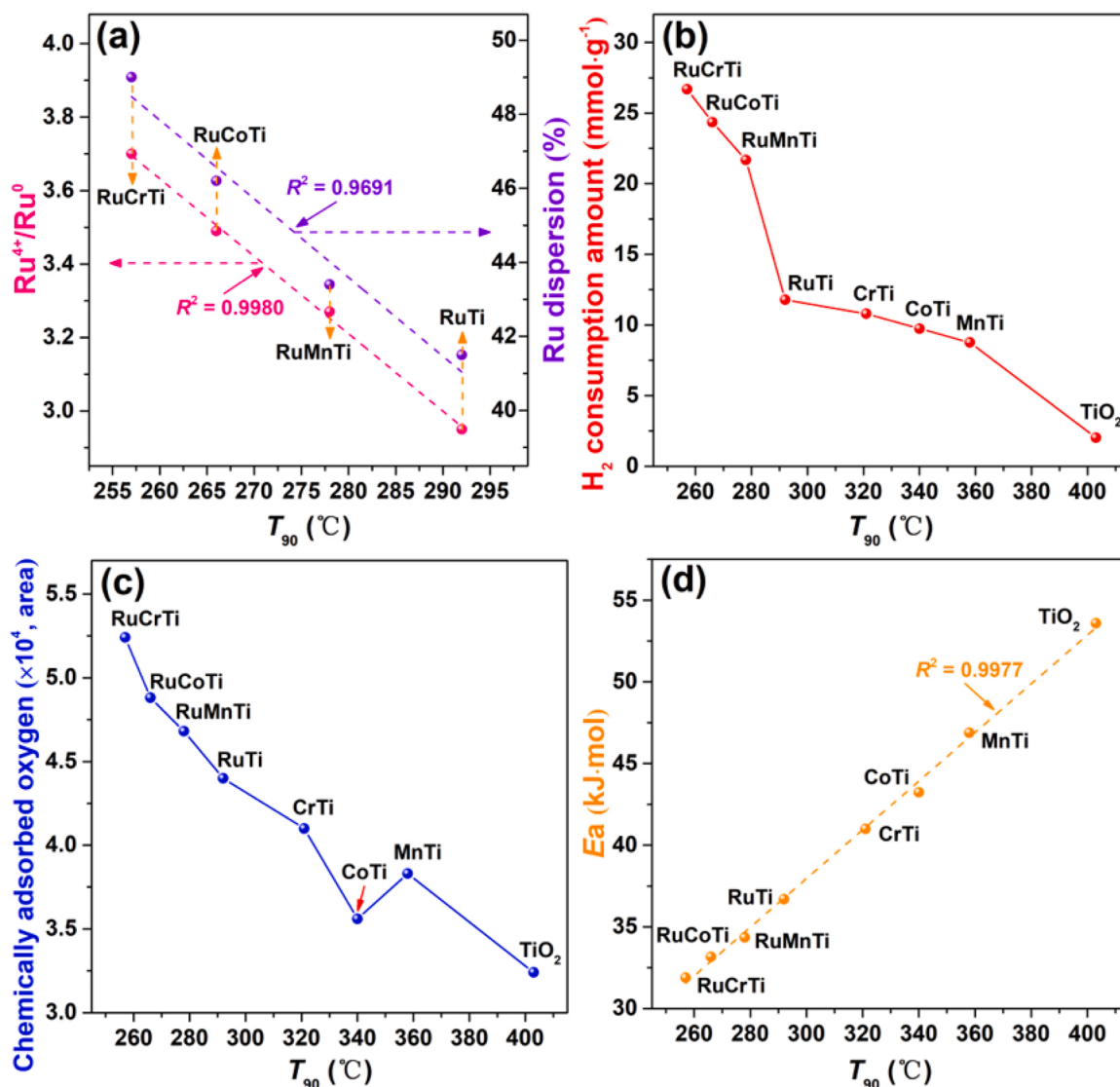
Fig. 8. (a) Relationship between catalytic activity and Ru^{4+}/Ru^0 ratio (or dispersion of Ru); (b) Relationship between catalytic activity and H_2 consumption amount; (c) Relationship between catalytic activity and chemically adsorbed oxygen; (d) Relationship between catalytic activity and apparent activation energy.

bands at 1126–1115 cm^{-1} corresponding to the vibration of -CH- can be only observed over RuCoTi and RuMnTi catalysts [20,22].

Based on the above information, a plausible reaction route and chlorine-resistance mechanism for RuCrTi catalyst in 1,2-DCE degradation were proposed (Scheme 1). 1,2-DCE molecules are rapidly adsorbed and activated on the surface of active sites (RuO$_2$ (main) and Cr$_2$O$_3$) at initial temperature (90–120 °C). With the increasing of temperature, 1,2-DCE molecules (adsorbed and activated over LAS) are decomposed through C-Cl bonds dissociation (forming the C$_2$H$_3$Cl) and C-C dissociation (forming the CH$_3$Cl; the cleavage of C-C bonds is the main reaction), and then rapidly transfer to polychlorinated by-products (CH$_2$Cl$_2$, CHCl$_3$, CCl$_4$ and C$_2$H$_3$Cl$_3$) by dehydrochlorination and chlorination [3,20,22]. The dissociated chlorine species are originated due to C-Cl bonds breakage, and most of the dissociated chlorine species are associated with H (from H$_2$O) to form HCl [43]. Additionally, the abundant surface hydroxyl groups are also as the hydrogen donor to facilitate HCl formation [49]. The high selective for inorganic chlorine species (HCl and Cl$_2$) indicates that abundant chlorine species on the surface of catalysts are released, and a little part of chlorine species attaches on the surface of catalyst and participate in the generation of chlorinated by-products. The larger amounts of chlorine species are efficiently removed, and intermediates (formate and carbonate species which regarded as the main sources of CO$_2$ and CO) generation are further promoted [20,22]. Finally, the intermediates are completely oxidized to CO, CO$_2$, HCl, Cl$_2$ and H$_2$O. The presence of the chlorine species over the used catalyst demonstrated that Cr$_2$O$_3$ is chlorinated to CrO$_x$Cl$_y$ because of oxygen substitution by chlorine (Fig. S7). Subsequently, CrO$_x$Cl$_y$ is re-oxidized by surface active oxygen species from RuO$_2$, resulting in the transfer of chlorine species from Cr$_2$O$_3$ to RuO$_2$ at relatively low temperature, avoiding the temperature window of the Deacon reaction and accelerating the removal and release of chlorine species [43].

3.5.3. Key factors determining catalytic performance

Reducibility, chemically adsorbed oxygen species, RuO$_2$ species and metal-support synergy effects of catalysts are generally considered as the parameters that influence the catalytic activity. Therefore, the T_{90} as a function of H$_2$ consumption amounts, chemically adsorbed oxygen and Ru^{4+}/Ru^0 of prepared catalysts were performed. As shown in Fig. 8a, T_{90} of catalysts correlate negatively to the ratio of Ru^{4+}/Ru^0 for RuTi and RuMTi catalysts ($R^2 = 0.9980$). That is, T_{90} of catalysts decrease with the increasing of the Ru^{4+}/Ru^0 ratio, indicating that large amounts of RuO$_2$ species with strong oxidizing ability can promote 1,2-DCE destruction due to the chlorine species can be opportunely removed from catalyst surface (Table 1) [3]. Moreover, T_{90} of catalysts correlate negatively to the dispersion of Ru ($R^2 = 0.9691$), illustrating that high Ru dispersion benefits to catalytic activity. Hence, the above results confirmed that Ru (Ru^{4+} and the dispersion of Ru) species serve a dominant role for 1,2-DCE deep oxidation. Combining the results in Tables 1 and 2, both the Ru^{4+}/Ru^0 ratio and TOF_{Ru} over RuCrTi are significantly increased compared to RuCoTi, RuMnTi and RuTi catalysts, demonstrating that Cr$_2$O$_3$ species are more favorable to promoting the formation of Ru^{4+} species than those of Co$_3$O$_4$ and Mn$_3$O$_4$ species. As displayed in Fig. 8b, RuCrTi has the highest H$_2$ consumption amount and 1,2-DCE oxidation activity, and T_{90} of catalysts correlate negatively to H$_2$ consumption amount of all catalysts, suggesting that reducibility of the catalysts plays a dominant role in 1,2-DCE destruction, which can be also verified by the results of reducibility and activity (Figs. 3a, 4a and S4a) [3]. Compared to Co$_3$O$_4$ and Mn$_3$O$_4$, Cr$_2$O$_3$ apparently enhance the reducibility of RuTi and accelerate 1,2-DCE decomposition at low temperature (Fig. 8b and Tables 1 and 2). Fig. 8c reveals that T_{90} of catalysts increases with the decreasing of chemically adsorbed oxygen for all catalysts (except MnTi). According to the results, it can be found that the abundant chemically adsorbed oxygen species can promote the cleavage of C-C and C-Cl bonds and therefore accelerate 1,2-DCE destruction [41]. In addition, the introduction of Cr$_2$O$_3$ species in RuTi induces more

chemically adsorbed oxygen species than that of RuCoTi, RuMnTi and RuTi catalysts (Table 1), which is a vital role in 1,2-DCE destruction. Overall, the presence of Cr$_2$O$_3$ species prominent improves the reducibility of RuTi and promotes the formation of active Ru^{4+} species and chemically adsorbed oxygen, which facilitates the degradation of 1,2-DCE at low temperature. Additionally, the relationship between E_a and activity is also presented in Fig. 8d. T_{90} of catalysts correlates positively to apparent activation energy ($R^2 = 0.9977$), revealing that apparent activation energy can reflect the catalytic capacity of catalysts.

4. Conclusions

In this work, a highly efficient RuO$_2$/Cr$_2$O$_3$/TiO$_2$ composite catalyst was developed and adopted for 1,2-DCE degradation. The Cr species not only as the second active sites, also as an auxiliary increases the reducibility of RuO$_2$/TiO$_2$ and promotes the formation of Ru^{4+} species (the main active sites) and chemically adsorbed oxygen, accelerating the degradation of 1,2-DCE at low temperature. 1,2-DCE is mainly dissociated and activated on the Lewis acid sites (Cr^{6+} and Ru^{4+}) over RuO$_2$/Cr$_2$O$_3$/TiO$_2$, resulting in the cleavage of C-Cl bonds and initiation of dehydrochlorination reaction (forming C$_2$H$_3$Cl). Whilst, CH$_2$Cl$_2$, CHCl$_3$ and CCl$_4$ also form through dehydrochlorination and chlorination (C-C cleavage). The presence of Cr species in RuO$_2$/TiO$_2$ obviously enhanced the amounts of Lewis acid sites and redox ability, facilitating the deep oxidation of 1,2-DCE and inhibiting the formation of CH$_2$Cl$_2$, C$_2$HCl$_3$ and CHCl$_3$ by-products. The RuO$_2$/Cr$_2$O$_3$/TiO$_2$ exhibits excellent resistance to H$_2$O, SO$_2$ and Cl species under simulated conditions. This work provides critical insights for the design of efficient materials for industrial CVOC degradation.

CRediT authorship contribution statement

All persons who have made substantial contributions to the work reported in the manuscript approved the final version. **Yu Huang** and **Mingjiao Tian** carried out the preparation of materials as well as performed the experiments of catalytic evaluation, catalyst characterizations and wrote the original manuscript; **Zeyu Jiang**, **Mudi Ma**, and **Changwei Chen** performed the HR-TEM and *in-situ* DRIFTs experiments; **Han Xu**, **Jingjie Zhang** and **Reem Albilali** assisted with writing and reviewing the manuscript; **Chi He** is supervision, who conceived the project, directed the study, analyzed the data, and assisted with writing the manuscript.

Declaration of Competing Interest

The authors declare that they have no known competing financial interests or personal relationships that could have appeared to influence the work reported in this paper.

Acknowledgements

Appendix A. Supporting information

References

[1] F. Lin, Z. Zhang, N. Li, B. Yan, C. He, Z. Hao, G. Chen, How to achieve complete elimination of Cl-VOCs: A critical review on byproducts formation and inhibition strategies during catalytic oxidation, Chem. Eng. J. 404 (2021), 126534.

[2] X. Xing, N. Li, J. Cheng, Y. Sun, G. Wang, Z. Zhang, H. Xu, C. He, Z. Hao, Hydrotalcite-Derived Cu$_x$Mg$_{3-x}$AlO Oxides for Catalytic Degradation of n-Butylamine with Low Concentration NO and Pollutant-Destruction Mechanism, Ind. Eng. Chem. Res. 58 (2019) 9362–9371.

[3] X. Zhang, Y. Liu, J. Deng, L. Jing, X. Yu, Z. Han, H. Dai, Effect of transition metal oxide doping on catalytic activity of titania for the oxidation of 1,2-dichloroethane, Catal. Today 375 (2021) 623–634.

[4] J. Su, Y. Liu, W. Yao, Z. Wu, Catalytic Combustion of Dichloromethane over HZSM-5-Supported Typical Transition Metal (Cr, Fe, and Cu) Oxide Catalysts: A Stability Study, J. Phys. Chem. C. 120 (2016) 18046–18054.

[5] Y. Su, K. Fu, Y. Zheng, N. Ji, C. Song, D. Ma, X. Lu, R. Han, Q. Liu, Catalytic oxidation of dichloromethane over Pt-Co/HZSM-5 catalyst: Synergistic effect of single-atom Pt, Co$_3$O$_4$, and HZSM-5, Appl. Catal. B: Environ. 288 (2021), 119980.

[6] T. Cai, H. Huang, W. Deng, Q. Dai, W. Liu, X. Wang, Catalytic combustion of 1,2-dichlorobenzene at low temperature over Mn-modified Co$_3$O$_4$ catalysts, Appl. Catal. B: Environ. 166–167 (2015) 393–405.

[7] L. Liu, J. Sun, J. Ding, Y. Zhang, J. Jia, T. Sun, Catalytic Oxidation of VOCs over SmMnO$_3$ Perovskites: Catalyst Synthesis, Change Mechanism of Active Species, and Degradation Path of Toluene, Inorg. Chem. 58 (2019) 14275–14283.

[8] P. Yang, S. Yang, Z. Shi, Z. Meng, R. Zhou, Deep oxidation of chlorinated VOCs over CeO$_2$-based transition metal mixed oxide catalysts, Appl. Catal. B: Environ. 162 (2015) 227–235.

[9] L.F. Liotta, Catalytic oxidation of volatile organic compounds on supported noble metals, Appl. Catal. B: Environ. 100 (2010) 403–412.

[10] S. Cao, X. Fei, Y. Wen, Z. Sun, H. Wang, Z. Wu, Bimodal mesoporous TiO$_2$ supported Pt, Pd and Ru catalysts and their catalytic performance and deactivation mechanism for catalytic combustion of Dichloromethane (CH$_2$Cl$_2$), Appl. Catal. A: Gen. 550 (2018) 20–27.

[11] B. Miranda, E. Díaz, S. Ordóñez, A. Vega, F.V. Díez, Performance of alumina-supported noble metal catalysts for the combustion of trichloroethene at dry and wet conditions, Appl. Catal. B: Environ. 64 (2006) 262–271.

[12] X. Liu, L. Chen, T. Zhu, R. Ning, Catalytic oxidation of chlorobenzene over noble metals (Pd, Pt, Ru, Rh) and the distributions of polychlorinated by-products, J. Hazard. Mater. 363 (2019) 90–98.

[13] C. Wang, N. Liu, C. Zhang, X. Liu, X. Li, X.S. Zhao, Ruthenium/cobalt binary oxides supported on hollow alumina microspheres as highly efficient catalyst for vinyl chloride oxidation, Appl. Surf. Sci. 497 (2019), 143776.

[14] Y. Yang, H. Li, S. Zhang, X. Yu, S. Liu, R. Qu, C. Zheng, X. Gao, Different reactive behaviours of dichloromethane over anatase TiO$_2$ supported RuO$_2$ and V$_2$O$_5$, Catal. Today 355 (2020) 349–357.

[15] N. Ye, Y. Li, Z. Yang, J. Zheng, S. Zuo, Rare earth modified kaolin-based Cr$_2$O$_3$ catalysts for catalytic combustion of chlorobenzene, Appl. Catal. A: Gen. 579 (2019) 44–51.

[16] W. Deng, Q. Dai, Y. Lao, B. Shi, X. Wang, Low temperature catalytic combustion of 1,2-dichlorobenzene over CeO$_2$-TiO$_2$ mixed oxide catalysts, Appl. Catal. B: Environ. 181 (2016) 848–861.

[17] H. Gai, X. Liu, B. Feng, C. Gai, T. Huang, M. Xiao, H. Song, An alternative scheme of biological removal of ammonia nitrogen from wastewater-highly dispersed Ru cluster @mesoporous TiO$_2$ for the catalytic wet air oxidation of low-concentration ammonia, Chem. Eng. J. 407 (2021), 127082.

[18] J. He, W. Li, P. Xu, J. Sun, Tuning electron correlations of RuO$_2$ by co-doping of Mo and Ce for boosting electrocatalytic water oxidation in acidic media, Appl. Catal. B: Environ. 298 (2021), 120528.

[19] M. Tian, Y. Jian, M. Ma, C. He, C. Chen, C. Liu, J.-W. Shi, Rational design of CrO$_x$/LaSrMnCoO$_6$ composite catalysts with superior chlorine tolerance and stability for 1,2-dichloroethane deep destruction, Appl. Catal. A: Gen. 570 (2019) 62–72.

[20] X. Feng, M. Tian, C. He, L. Li, J.-W. Shi, Y. Yu, J. Cheng, Yolk-shell-like mesoporous CoCrO$_x$ with superior activity and chlorine resistance in dichloromethane destruction, Appl. Catal. B: Environ. 264 (2020) 118493.

[21] J. Wang, C. Wang, M. Zhen, Template-free synthesis of multifunctional Co$_3$O$_4$ nanotubes as excellent performance electrode materials for superior energy storage, Chem. Eng. J. 356 (2019) 1–10.

[22] M. Tian, X. Guo, R. Dong, Z. Guo, J. Shi, Y. Yu, M. Cheng, R. Albilali, C. He, Insight into the boosted catalytic performance and chlorine resistance of nanosphere-like meso-macroporous CrO$_x$/MnCo$_3$O$_x$ for 1,2-dichloroethane destruction, Appl. Catal. B: Environ. 259 (2019), 118018.

[23] K.A. Alzahrani, R.M. Mohamed, A.A. Ismail, Enhanced visible light response of heterostructured Cr$_2$O$_3$ incorporated two-dimensional mesoporous TiO$_2$ framework for H2 evolution, Ceram. Int 47 (2021) 21293–21302.

[24] J.R. Rajabathar, P. Arunachalam, Z.A. Issa, T. Ahmed M, Synthesis and characterization of novel metal chalcogenide modified Ni-Co-MnO$_2$ nanofibers rolled with graphene based visible light active catalyst for nitro phenol degradation, Optik 224 (2020), 165538.

[25] X. Yao, L. Zhang, L. Li, L. Liu, Y. Cao, X. Dong, F. Gao, Y. Deng, C. Tang, Z. Chen, L. Dong, Y. Chen, Investigation of the structure, acidity, and catalytic performance of CuO/Ti$_{0.95}$Ce$_{0.05}$O$_2$ catalyst for the selective catalytic reduction of NO by NH$_3$ at low temperature, Appl. Catal. B: Environ. 150–151 (2014) 315–329.

[26] X. Yao, R. Zhao, L. Chen, J. Du, C. Tao, F. Yang, L. Dong, Selective catalytic reduction of NO$_x$ by NH$_3$ over CeO$_2$ supported on TiO$_2$: Comparison of anatase, brookite, and rutile, Appl. Catal. B: Environ. 208 (2017) 82–93.

[27] H. Wang, X. Li, Q. Ruan, J. Tang, Ru and RuO$_x$ decorated carbon nitride for efficient ammonia photosynthesis, Nanoscale 12 (2020) 12329–12335.

[28] L.F. Nascimento, R.F. Martins, O.A. Serra, Catalytic combustion of soot over Ru-doped mixed oxides catalysts, J. Rare Earth. 32 (2014) 610–620.

[29] L. Liu, K. Xu, S. Su, L. He, M. Qing, H. Chi, T. Liu, S. Hu, Y. Wang, J. Xiang, Efficient Sm modified Mn/TiO$_2$ catalysts for selective catalytic reduction of NO with NH$_3$ at low temperature, Appl. Catal. A: Gen. 592 (2020), 117413.

[30] J. González-Prior, R. López-Fonseca, J.I. Gutiérrez-Ortiz, B. de Rivas, Oxidation of 1,2-dichloroethane over nanocube-shaped Co$_3$O$_4$ catalysts, Appl. Catal. B: Environ. 199 (2016) 384–393.

[31] H. Zhao, F. Dong, W. Han, Z. Tang, Study of Morphology-Dependent and Crystal-Plane Effects of CeMnO$_x$ Catalysts for 1,2-Dichlorobenzene Catalytic Elimination, Ind. Eng. Chem. Res. 58 (2019) 18055–18064.

[32] R. Fang, R. Huang, J. Ji, M. He, Q. Feng, Y. Zhan, D.Y.C. Leung, Efficient MnO$_x$ supported on coconut shell activated carbon for catalytic oxidation of indoor formaldehyde at room temperature, Chem. Eng. J. 334 (2018) 2050–2057.

[33] F. Wang, C. Li, X. Zhang, M. Wei, D.G. Evans, X. Duan, Catalytic behavior of supported Ru nanoparticles on the {100}, {110}, and {111} facet of CeO$_2$, J. Catal. 329 (2015) 177–186.

[34] R. Wang, Y. Wang, M. Ren, G. Sun, D. Gao, Y.R. Chin Chong, X. Li, G. Chen, Effect of ceria morphology on the catalytic activity of Ru/ceria for the dehydrogenation of ammonia borane, Int. J. Hydrog. Energ. 42 (2017) 6757–6764.

[35] M. Tian, C. He, Y. Yu, H. Pan, L. Smith, Z. Jiang, N. Gao, Y. Jian, Z. Hao, Q. Zhu, Catalytic oxidation of 1,2-dichloroethane over three-dimensional ordered meso-macroporous Co$_3$O$_4$/La$_{0.7}$Sr$_{0.3}$Fe$_{0.5}$Co$_{0.5}$O$_3$: Destruction route and mechanism, Appl. Catal. A: Gen. 553 (2018) 1–14.

[36] Q. Dai, S. Bai, Z. Wang, X. Wang, G. Lu, Catalytic combustion of chlorobenzene over Ru-doped ceria catalysts, Appl. Catal. B: Environ. 126 (2012) 64–75.

[37] P. Yang, S. Zuo, Z. Shi, F. Tao, R. Zhou, Elimination of 1,2-dichloroethane over (Ce, Cr)$_x$O$_2$/MO$_y$ catalysts (M = Ti, V, Nb, Mo, W and La), Appl. Catal. B: Environ. 191 (2016) 53–61.

[38] Z. Zheng, Y. Yang, H. Li, Q. Xin, S. Zhang, Y. Liu, S. Liu, C. Zheng, H. Song, X. Gao, Effect of multi-pollutant on the catalytic oxidation of dichloromethane over RuO$_2$-WO$_3$/Sn$_{0.2}$Ti$_{0.8}$O$_2$ catalyst, Fuel 278 (2020), 118207.

[39] S. Cao, H. Wang, F. Yu, M. Shi, S. Chen, X. Weng, Y. Liu, Z. Wu, Catalyst performance and mechanism of catalytic combustion of dichloromethane (CH$_2$Cl$_2$) over Ce doped TiO$_2$, J. Colloid Interface Sci. 463 (2016) 233–241.

[40] Y. Gu, X. Jiang, W. Sun, S. Bai, Q. Dai, X. Wang, 1,2-Dichloroethane Deep Oxidation over Bifunctional Ru/Ce$_x$Al$_y$ Catalysts, ACS Omega 3 (2018) 8460–8470.

[41] L. Zhu, S. Pan, Z. Liu, P. Wei, Z. Liu, P. Yu, Y. Xu, Effect of Rare Earth Metal (RE = La, Pr, Nd, Y) Doping on Co-Ce Composite Oxide and Its Application in Catalytic Combustion of Chlorobenzene, Ind. Eng. Chem. Res. 59 (2020) 5686–5698.

[42] H. Xia, Y. Chen, J. Wu, S. Shao, G. Chen, H. Zhang, Q. Dai, X. Wang, Oxidative decomposition of chlorobenzene over iron titanate catalysts: The critical roles of oxygen vacancies and adsorption geometries, Appl. Catal. A: Gen. 617 (2021), 118118.

[43] Q. Dai, J. Wu, W. Deng, J. Hu, Q. Wu, L. Guo, W. Sun, W. Zhan, X. Wang, Comparative studies of P/CeO$_2$ and Ru/CeO$_2$ catalysts for catalytic combustion of dichloromethane: From effects of H$_2$O to distribution of chlorinated by-products, Appl. Catal. B: Environ. 249 (2019) 9–18.

[44] Y. Gu, T. Cai, X. Gao, H. Xia, W. Sun, J. Zhao, Q. Dai, X. Wang, Catalytic combustion of chlorinated aromatics over WO$_x$/CeO$_2$ catalysts at low temperature, Appl. Catal. B: Environ. 248 (2019) 264–276.

[45] W. Wang, Q. Zhu, Q. Dai, X. Wang, Fe doped CeO$_2$ nanosheets for catalytic oxidation of 1,2-dichloroethane: Effect of preparation method, Chem. Eng. J. 307 (2017) 1037–1046.

[46] Q. Dai, H. Huang, Y. Zhu, W. Deng, S. Bai, X. Wang, G. Lu, Catalysis oxidation of 1,2-dichloroethane and ethyl acetate over ceria nanocrystals with well-defined crystal planes, Appl. Catal. B: Environ. 117–118 (2012) 360–368.

[47] Y. Huang, S. Fang, M. Tian, Z. Jiang, Y. Wu, C. He, Chlorine-Resistant Hollow Nanosphere-Like VO$_x$/CeO$_2$ Catalysts for Highly Selective and Stable Destruction of 1,2-Dichloroethane: Byproduct Inhibition and Reaction Mechanism, Processes 9 (2021) 119.

[48] Z. Zhang, J. Huang, H. Xia, Q. Dai, Y. Gu, Y. Lao, X. Wang, Chlorinated volatile organic compound oxidation over SO$_4^{2-}$/Fe$_2$O$_3$ catalysts, J. Catal. 360 (2018) 277–289.

[49] Y. Jiao, X. Chen, F. He, S. Liu, Simple preparation of uniformly distributed mesoporous Cr/TiO$_2$ microspheres for low-temperature catalytic combustion of chlorobenzene, Chem. Eng. J. 372 (2019) 107–117.